NeuroImage 264 (2022) 119763

Contents lists available at ScienceDirect

NeuroImage

journal homepage: www.elsevier.com/locate/neuroimage

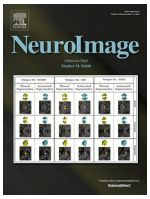

An optimized reference tissue method for quantification of tau protein depositions in diverse neurodegenerative disorders by PET with ^{18}F-PM-PBB3 (^{18}F-APN-1607)

Kenji Tagai[a,b,1,*], Yoko Ikoma[a,1], Hironobu Endo[a], Oiendrila Bhowmik Debnath[a], Chie Seki[a], Kiwamu Matsuoka[a], Hideki Matsumoto[a], Masaki Oya[a], Kosei Hirata[a], Hitoshi Shinotoh[a], Keisuke Takahata[a,c], Shin Kurose[a,c], Yasunori Sano[a,c], Maiko Ono[a], Hitoshi Shimada[a,d], Kazunori Kawamura[a], Ming-Rong Zhang[a], Yuhei Takado[a,*], Makoto Higuchi[a]

[a] *Quantum Life and Medical Science Directorate, National Institutes for Quantum Science and Technology, Institute for Quantum Medical Science, Chiba 263-8555, Japan*

[b] *Department of Psychiatry, The Jikei University of Medicine, Tokyo 105-8461, Japan*

[c] *Department of Psychiatry, Keio University School of Medicine, Tokyo 160-0016, Japan*

[d] *Department of Functional Neurology & Neurosurgery, Center for Integrated Human Brain Science, Brain Research Institute, Niigata University, Niigata 951-8585, Japan*

ARTICLE INFO

Keywords:
Tau PET
Reference tissues
Alzheimer's disease
Progressive supranuclear palsy
Frontotemporal lobar degeneration

ABSTRACT

Positron emission tomography (PET) with ^{18}F-PM-PBB3 (^{18}F-APN-1607, ^{18}F-Florzolotau) enables high-contrast detection of tau depositions in various neurodegenerative dementias, including Alzheimer's disease (AD) and frontotemporal lobar degeneration (FTLD). A simplified method for quantifying radioligand binding in target regions is to employ the cerebellum as a reference (CB-ref) on the assumption that the cerebellum has minimal tau pathologies. This procedure is typically valid in AD, while FTLD disorders exemplified by progressive supranuclear palsy (PSP) are characterized by occasional tau accumulations in the cerebellum, hampering the application of CB-ref. The present study aimed to establish an optimal method for defining reference tissues on ^{18}F-PM-PBB3-PET images of AD and non-AD tauopathy brains. We developed a new algorithm to extract reference voxels with a low likelihood of containing tau deposits from gray matter (GM-ref) or white matter (WM-ref) by a bimodal fit to an individual, voxel-wise histogram of the radioligand retentions and applied it to ^{18}F-PM-PBB3-PET data obtained from age-matched 40 healthy controls (HCs) and 23 CE, 40 PSP, and five other tau-positive FTLD patients. PET images acquired at 90–110 min after injection were averaged and co-registered to corresponding magnetic resonance imaging space. Subsequently, we generated standardized uptake value ratio (SUVR) images estimated by CB-ref, GM-ref and WM-ref, respectively, and then compared the diagnostic performances. GM-ref and WM-ref covered a broad area in HCs and were free of voxels located in regions known to bear high tau burdens in AD and PSP patients. However, radioligand retentions in WM-ref exhibited age-related declines. GM-ref was unaffected by aging and provided SUVR images with higher contrast than CB-ref in FTLD patients with suspected and confirmed corticobasal degeneration. The methodology for determining reference tissues as optimized here improves the accuracy of ^{18}F-PM-PBB3-PET measurements of tau burdens in a wide range of neurodegenerative illnesses.

1. Introduction

Depositions of tau fibrils in the brain are the hallmarks of Alzheimer's disease (AD) and a significant subset of frontotemporal lobar degeneration (FTLD), including progressive supranuclear palsy (PSP), corticobasal degeneration (CBD), and Pick's disease (PiD). The structures of tau in these and other diverse tauopathies are distinct (Buee et al., 2000; Shi et al., 2021), and they determine the subcellular, cellular, and regional distribution of tau aggregates in close relationships with clinical phenotypes (Arima, 2006; Delacourte, 2005).

The recent development of radioligands for positron emission tomography (PET) has enabled *in vivo* visualization of tau fibril depositions (Villemagne et al., 2018; Leuzy et al., 2019). To quantify tau accumulations in AD brains, a ratio of the radioactivity uptake between target

* Corresponding authors.
E-mail addresses: tagai.kenji@qst.go.jp (K. Tagai), takado.yuhei@qst.go.jp (Y. Takado).

[1] These authors contributed equally to this work.

https://doi.org/10.1016/j.neuroimage.2022.119763.
Received 14 February 2022; Received in revised form 15 October 2022; Accepted 21 November 2022
Available online 24 November 2022.

and reference tissue defined as standardized uptake value ratio (SUVR) or distribution volume ratio is often employed as a simplified index for the specific probe binding to tau aggregates under the assumption that the reference region is devoid of tau lesions harboring binding components. Similarly, time-radioactivity curves in the target and reference regions are comparatively utilized for the estimation of non-displaceable binding potential (BP_{ND}) of the radiotracer according to pharmacokinetic models. The reference tissue is primarily defined on cerebellar gray matter (CB-ref) for PET measurements of AD-type tau pathologies since this anatomical structure is considered to contain minimal tau fibrils in AD (Barret et al., 2017; Pascoal et al., 2018; Kuwabara et al., 2018; Mueller et al., 2020).

While most PET probes for tau deposits are incapable of sensitive detection of FTLD-type tau assemblies formed by a subgroup of tau isoforms, we developed a PET ligand, ^{11}C-PBB3, for visualizing AD and non-AD tau pathologies, including PSP-, CBD-, and PiD-type tau inclusions (Maruyama et al., 2013). ^{11}C-PBB3 did not yield abundant radiosignals in the brain due to its high propensity to metabolic conversions and consequent inefficiency of its transfer to the brain, but a fluorinated analog of ^{11}C-PBB3, ^{18}F-PM-PBB3 (also known as ^{18}F-APN-1607 or ^{18}F-Florzolotau), displayed improved biostability and allowed detection of a wide range of tau lesions with high contrast (Tagai et al., 2021). The use of CB-ref might lead to underestimation of the radiotracer binding in target tissues, particularly in patients with PSP and CBD, as tau pathologies could exist in the cerebellum of these cases (Kimura et al., 2016; Endo et al., 2019). To circumvent this technical issue, we extracted reference voxels with a low likelihood of tau depositions from gray matter in parametric images based on whether the voxel-wise BP_{ND} was within a range assigned using a histogram in healthy controls (Kimura et al., 2016). This method was applied to determining BP_{ND} of ^{11}C-PBB3 in subjects with AD (Kimura et al., 2016), PSP (Endo et al., 2019), and several other non-AD tauopathies (Shinotoh et al., 2019; Takahata et al., 2019). More recently, other research groups developed a procedure to extract reference voxels from white matter based on whether the voxel-wise radiotracer retention was included in a range assigned using an individual histogram (Southekal et al., 2018; Zhang et al., 2021). This methodology was then applied in the estimation of ^{18}F-PM-PBB3 retention in AD cases (Zhang et al., 2021), and the employment of individual histograms allowed handy quantitative assays without generating an average histogram in control subjects. However, it remains unclear whether reference voxels should be collected from gray or white matter, and it also needs to be determined how the range of the probe retention in the histogram is selected for the reference extraction.

The present study aims to establish an optimal method to define reference voxels for the quantification of ^{18}F-PM-PBB3 binding in diverse tauopathies. We constructed a new workflow to assign the range of the probe uptake for picking up adequate voxels with sufficient robustness in consideration of diverse histogram profiles. Then, the accuracy of diagnostic discriminations and contrasts for tau pathologies were compared among CB-ref and pools of reference voxels extracted from gray matter (GM-ref) and white matter (WM-ref).

2. Methods

2.1. Participants

We analyzed age-matched datasets of 40 healthy controls (HCs), 23 patients with AD, 40 patients with PSP, and five patients with other FTLD syndromes. These datasets were acquired from clinical studies registered in the UMIN Clinical Trials Registry (UMIN–CTR; IDs 000030248, 000034546, 000033808, 000030319). They were approved by the Radiation Drug Safety Committee and National Institutes for Quantum Science and Technology Certified Review Board of Japan. Written informed consent was obtained from all subjects and/or from close family members when subjects were cognitively impaired.

Table 1
Demographic data.

	HC	AD	PSP
Demographics			
Number	40	23	40
Age	68.6 (5.7)	66.2 (10.0)	70.4 (6.4)
Gender (male/female)	25/15	11/12	22/18
MMSE	28.3 (1.5)	21.8 (3.7) *,†	24.8 (4.6) *
PSPRS	N/A	N/A	38.1 (18.2)
PiB SUVR	1.07 (0.08)	2.03 (0.31)**	1.14 (0.17)
Volumes of reference (cm^3)			
CB-ref	62.8 (7.3)	65.3 (11.1)	60.4 (9.7)
GM-ref	124.6 (31.0)	52.5 (21.6) *,†	95.8 (36.2) *
WM-ref	157.6 (28.1)	144.8 (26.9)	142.8 (29.4) *

HC, healthy control; AD, Alzheimer's disease; PSP, progressive supranuclear palsy; MMSE, mini-mental state examination; PSPRS, progressive supranuclear palsy rating scale; SUVR, standardized uptake value ratio; CB-ref, cerebellar reference; GM-ref, gray matter reference; WM-ref, white matter reference.
PSP patients consisted of 33 PSP-Richardson and 7 PSP with other clinical phenotypes: PSP with progressive gait freezing (PSP-PGF), predominant parkinsonism (PSP-P), and predominant speech/ language disorder (PSP-SL).
Values are listed as mean ± standard deviation.
* , HC higher than AD and PSP, $P < 0.05$.
** , AD higher than HC and PSP, $P < 0.05$.
† , PSP higher than AD, $P < 0.05$.

All patients were clinically diagnosed according to the established criteria that we previously reported (Petersen et al., 1999; McKhann et al., 1984; Hoglinger et al., 2017; Armstrong et al., 2013; Rascovsky et al., 2011; Gorno-Tempini et al., 2011). Depositions of amyloid-beta (Aβ) were assessed by a visual inspection of ^{11}C-PiB-PET images (Tagai et al., 2021) and quantified as standardized uptake value ratio (SUVR) with the whole cerebellum as a reference region and the Centiloid atlas implemented in the PMOD Neuro Tool (PMOD Technologies Ltd). All AD patients were indicated by PET as having Aβ plaques and denoted as Aβ (+), and five Aβ (+) MCI patients were added to the AD group. The PSP group consisted of 33 patients with PSP Richardson syndrome (PSP-Richardson) with typical manifestations and seven patients with other clinical phenotypes (PSP-other). HCs were without a history of neurological and psychiatric disorders, and they were age-matched with the AD and PSP groups (Table 1). Patients with other FTLDs, including corticobasal degeneration syndrome (CBS), progressive non-fluent aphasia (PNFA), and behavioral variant of frontotemporal dementia (BvFTD), were also incorporated as in our previous report (Tagai et al., 2021), and two of these cases were neuropathologically diagnosed as having CBD and PiD by biopsy and autopsy, respectively (Klein and Tourville, 2012). All HCs, PSP, and other FTLD patients were Aβ (-) according to PET findings.

2.2. Image acquisition and data preprocessing

MR images were acquired with a 3-T scanner, MAGNETOM Verio (Siemens Healthcare). Three-dimensional T1-weighted gradient-echo sequence produced a gapless series of thin sagittal sections (TE = 1.95 ms, TR = 2300 ms, TI = 900 ms, flip angle = 9°, acquisition matrix = 512 × 512 × 176, voxel size = 1 × 0.488 × 0.488 mm). PET assays were conducted with a Biograph mCT Flow system (Siemens Healthcare), which provides 109 sections with an axial field of view of 16.2 cm. The intrinsic spatial resolution was 5.9 mm in-plane and 5.5 mm full-width at half-maximum axially. Images were reconstructed using a filtered back-projection algorithm with a Hanning filter (4.0 mm full-width at half-maximum). ^{18}F-PM-PBB3 was injected into the subjects at an average dose of 186.4 ± 8.2 MBq and a molar activity of 237.4 ± 75.3 GBq/μmol. The entire process from radiosynthesis to injection of ^{18}F-PM-PBB3 was performed under UV-cut light to avoid photoisomerization.

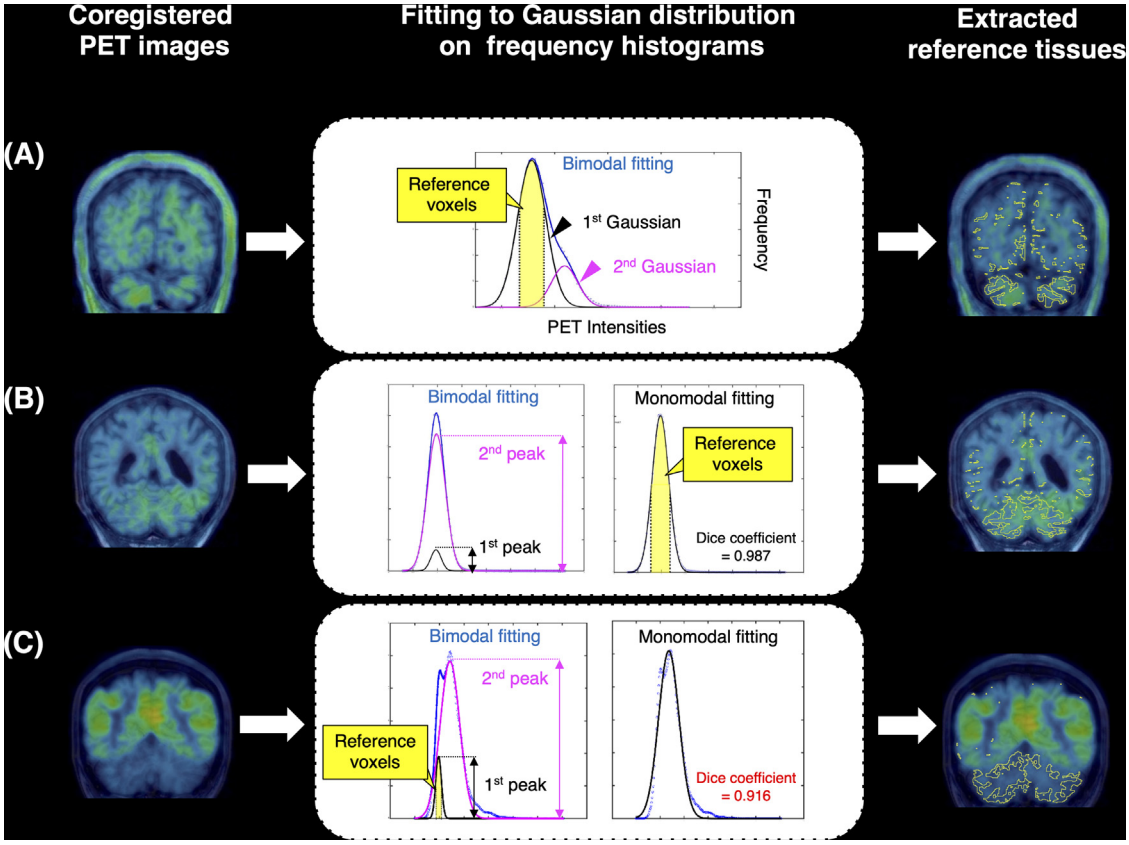

Fig. 1. Flowcharts of extracting reference tissues by developed algorithm on ^{18}F-PM-PBB3 PET images. The yellow-labeled regions show extracted references based on bimodal/monomodal Gaussian fitting, respectively. (A) A histogram obtained from a PSP-Richardson case, and the reference was extracted from the 1st Gaussian distribution based on bimodal fitting. (B) shows histograms obtained from a PSP-PGF case. The amplitude of the 1st peak was less than half of the 2nd peak on bimodal fitting (left), and the Dice coefficient was higher than the threshold value (>0.936) on monomodal fitting (right). Hence, the reference was set based on monomodal fitting. (C) shows histograms obtained from an AD case. The amplitude of the 1st peak was less than half of the 2nd peak on bimodal fitting (left), whereas the Dice coefficient was lower than the threshold value (<0.936) on monomodal fitting (right). Ultimately, the reference was set based on bimodal fitting.

Data preprocessing was performed using PMOD 3.8 (PMOD Technologies Ltd) and Statistical Parametric Mapping software (SPM12, Wellcome Department of Cognitive Neurology). Acquired PET images were corrected for head motions. Briefly, images at 100–110 min were aligned with a summation image at 90–100 min using PMOD 3.8. Then, motion-corrected PET images were rigidly co-registered to individual T1-weighted MR images. To generate SUVR images, we averaged PET data acquired at 90–110 min after radiotracer injection. In addition, the individual MR images were segmented, and the probability maps of gray matter (GM) and white matter (WM) were generated using SPM12 for the extraction of reference voxels based on histogram analysis.

2.3. Histogram-based definition of reference voxels

We propose a new method to define reference voxels in GM or WM based on the frequency histogram of voxel-counts with a homemade script implemented MATLAB (The Mathworks, Natick, MA, USA). In this procedure, the PERSI (Parametric Estimation of Reference Signal Intensity) method documented previously (Southekal et al., 2018) is modified to extract reference voxels from GM as well as WM and is further refined to select the optimal reference voxels by stable fits of Gaussian distributions to the histogram.

A binary mask image of GM or WM was generated from the probability maps by selecting voxels with a higher than 90% probability of being GM or WM after the erosion by morphological operation using $3 \times 3 \times 3$ neighboring voxels to eliminate the influence from boundary regions. Subsequently, a voxel-wise frequency histogram of voxel-counts was constructed from an individual PET image masked for GM or WM.

A bimodal Gaussian distribution fit was then applied to the histogram in light of the view that voxels with and without tau pathologies formed two distinct peaks (Southekal et al., 2018). The first Gaussian distribution with a lower-count peak was regarded to contain voxels with no or minimal tau deposits, and hence voxels with values within the full-width at half-maximum (FWHM) of this peak were extracted and pooled as a reference region. The extracted reference region was exported as a probability map as expressed in Eq. (2), and the representative value of tracer retention in the reference region (C_{ref}) was determined by averaging reference voxel values weighted for the probability of being contained in the first versus second Gaussian distribution (w_i) as follows:

$$C_{ref} = \sum_{i=1}^{N} w_i C_i / \sum_{i=1}^{N} w_i \quad (1)$$

$$w_i = g_1(C_i)/(g_1(C_i) + g_2(C_i)), \quad (2)$$

where C_i is the value of the i*th* voxel, g_1 and g_2 are the first and second Gaussian distribution functions, respectively, and N is the number of reference voxels (Fig. 1A).

If the height of the first peak was less than half of the second peak, we applied monomodal Gaussian distribution to the histogram to circumvent potential lack of the fitting robustness in the bimodal fit due to an insufficient number of voxels in the first peak (Fig. 1B). The monomodal Gaussian distribution fit was then evaluated by the Dice coefficient, which is a ratio of the area between the doubled intersection of the polygonized histogram and fitted Gaussian distribution and the sum of these two polygons. If the Dice coefficient was smaller than

the threshold value determined with HC data in the current cohort, the bimodal Gaussian distribution fit was considered more appropriate than the monomodal fit (Fig. 1C). The threshold was set at 0.936, which is the mean -2 standard deviation (SD) value of cases in which monomodal fitting was applied in HCs. In the use of the monomodal fit, C_{ref} was determined by averaging counts in all voxels within the FWHM (Fig. 1B). Finally, all voxel-counts were normalized by C_{ref} in GM-ref or WM-ref as well as retention in CB-ref (cerebellar cortex) labeled with Freesurfer 6.0 from the Desikan–Killiany–Tourville atlas as a conventional method (Klein and Tourville, 2012), to produce SUVR images, respectively.

2.4. Target regions

The target region was placed in an area with abundant tracer binding in AD and PSP patients, on the basis of previous studies (Tagai et al., 2021). We defined volumes of interest (VOIs) in the neocortex involved in AD tau pathologies at Braak stages V and VI (BraakV/VI) and inferior temporal cortex (ITC) and in the subthalamic nucleus (STN) burdened with PSP-type tau deposits. Braak V/VI VOI was applied for discrimination between HC and AD, STN VOI between HC and PSP, and ITC VOI between AD and PSP (Ossenkoppele et al., 2018), respectively. The Braak V/VI and ITC VOI were labeled using FreeSurfer 6.0 as described elsewhere. The STN VOI was defined with a template atlas (Talairach Daemon atlas from the Wake Forest University PickAtlas version 3.0.5) in the MNI (Montreal Neurologic Institute) space, and spatial normalization was conducted according to the Diffeomorphic Anatomical Registration Through Exponentiated Lie Algebra (DARTEL) algorithm. For other FTLDs, VOIs were also generated with FreeSurfer 6.0 in areas enriched with tau lesions characteristic of each disease, such as the precentral cortex in CBS and PNFA and the orbitofrontal cortex in BvFTD.

2.5. Statistical analyzes

Statistical examinations were performed using GraphPad Prism 9.0. We adapted Fisher's exact test (sex) and Kruskal-Wallis test (other parameters) for comparisons between HCs, AD, and PSP groups ($P < 0.05$, corrected by Dunn's multiple comparisons). The performance of the diagnosis based on SUVR values in the target VOIs against CB-ref, GM-ref, and WM-ref was evaluated using Mann-Whitney U test and area under the curve (AUC) values in Receiver Operating Characteristic (ROC) curves; differences in AUC values were examined by DeLong's method (Hanley and McNeil, 1983). Correlations of the age with radioligand SUVRs in each of the three reference tissues estimated with the other two references were also assessed by Spearman's rank-order method.

To directly compare SUVR values calculated with CB-ref and other references, we conducted linear regression analysis and assessed correlations between SUVR values of target regions estimated with these reference tissues. Furthermore, we performed voxel-wise comparisons of SUVRs determined with the different reference tissues by SPM12. The two-sample *t*-test model was applied to the comparisons between parametric SUVR images quantified with CB-ref and other references. For multiple voxel comparisons, family-wise error corrections at peak levels were applied ($p < 0.05$).

2.6. Data availability

Data supporting the findings of this study are available from the corresponding author upon reasonable request. Sharing and reuse of data require the expressed written permission of the authors, as well as clearance from the Institutional Review Boards.

3. Results

3.1. Evaluations of reference tissues

Table 1 shows the demographics of the subjects and volumes of defined CB-ref, GM-ref, and WM-ref. The bimodal Gaussian distribution fit to the histogram was judged as adequate in most cases, while the monomodal fit was chosen in GM histograms of six HCs and five PSP, and WM histograms of one HC and one AD case.

Table 2
Correlations between radioligand SUVRs in the three references and ages.

	CB-ref	GM-ref	WM-ref
Quantified by CB-ref	N/A	0.058	-0.291*
Quantified by GM-ref	-0.058	N/A	-0.351*
Quantified by WM-ref	0.291*	0.351*	N/A

CB-ref, cerebellar reference; GM-ref, gray matter reference; WM-ref, white matter reference.
Values indicate Spearman coefficients of correlations.
* , correlated with age, $P < 0.05$.

Table 3
AUC values in ROC analysis of the discriminations with SUVRs in the target regions quantified with the three reference tissues.

	CB-ref	GM-ref	WM-ref
HC versus AD	0.998	0.998	0.985
HC versus PSP	0.918	0.930	0.923
AD versus PSP	1.00	0.998	0.995

HC, healthy control; AD, Alzheimer's disease; PSP, progressive supranuclear palsy; CB-ref, cerebellar reference; GM-ref, gray matter reference; WM-ref, white matter reference.
AUC values estimated from ROC curve analyzes are displayed. Each of target region was set at BraakV/VI (HC versus AD), STN (HC versus PSP) and ITC (AD versus PSP), respectively.

Fig. 2A demonstrates representative images of GM-ref and WM-ref. As a result of Gaussian fitting, voxels in GM-ref showed a tendency to pick up from a broad area in HCs, the cerebellum in AD and PSP cases, except for several PSP cases showing high radioligand accumulation in the cerebellum. Meanwhile, voxels in WM-ref were extracted from extensive areas in HCs and AD cases and regions excluding a WM portion of the basal ganglia in PSP cases. Averaged GM-ref and WM-ref maps in each diagnostic group were in agreement with these findings (Fig. 2B and Supplementally Fig. 1). In particular, the spatial distributions of reference voxels with high probabilities in AD and PSP did not overlap with known tau topologies. Meanwhile, the tracer retentions in WM-ref estimated with CB-ref and GM-ref presented a negative correlation with aging, and the retentions in CB-ref and GM-ref estimated with WM-ref were positively correlated with ages (Table 2). These associations were also observed in the analysis restricted to HCs, who had no tau lesions (data not shown), indicating an age-related decline of the non-displaceable radioligand binding in WM-ref.

3.2. Diagnostic performance of quantifications with CB-ref, GM-ref, and WM-ref

Fig. 3 illustrates comparisons of SUVRs in the target VOIs among the AD, PSP, and HC groups. SUVRs generated with all three reference tissues exhibited significant differences between all three groups ($p < 0.05$, Fig. 3 and Supplementary Fig. 2), whereas the SD of these values estimated with WM-ref was higher than those estimated with CB-ref and GM-ref in HCs (Supplemental Table 1). Table 3 shows AUC values according to ROC curve analyzes. The use of CB-ref and GM-ref yielded high AUC values (= 0.998) relative to WM-ref (= 0.985) in the separation between AD patients and HCs. GM-ref also produced a higher AUC value (= 0.930) than WM-ref (= 0.923) and CB-ref (= 0.918) in the discrimination between PSP patients and HCs. WM-ref (= 0.995) also yielded lower AUC values than GM-ref (= 0.998) and CB-ref (= 1.00) in the discrimination between AD and PSP patients. However, there were no statistically significant differences between these AUC values ($p > 0.05$) (Supplementary Table 2).

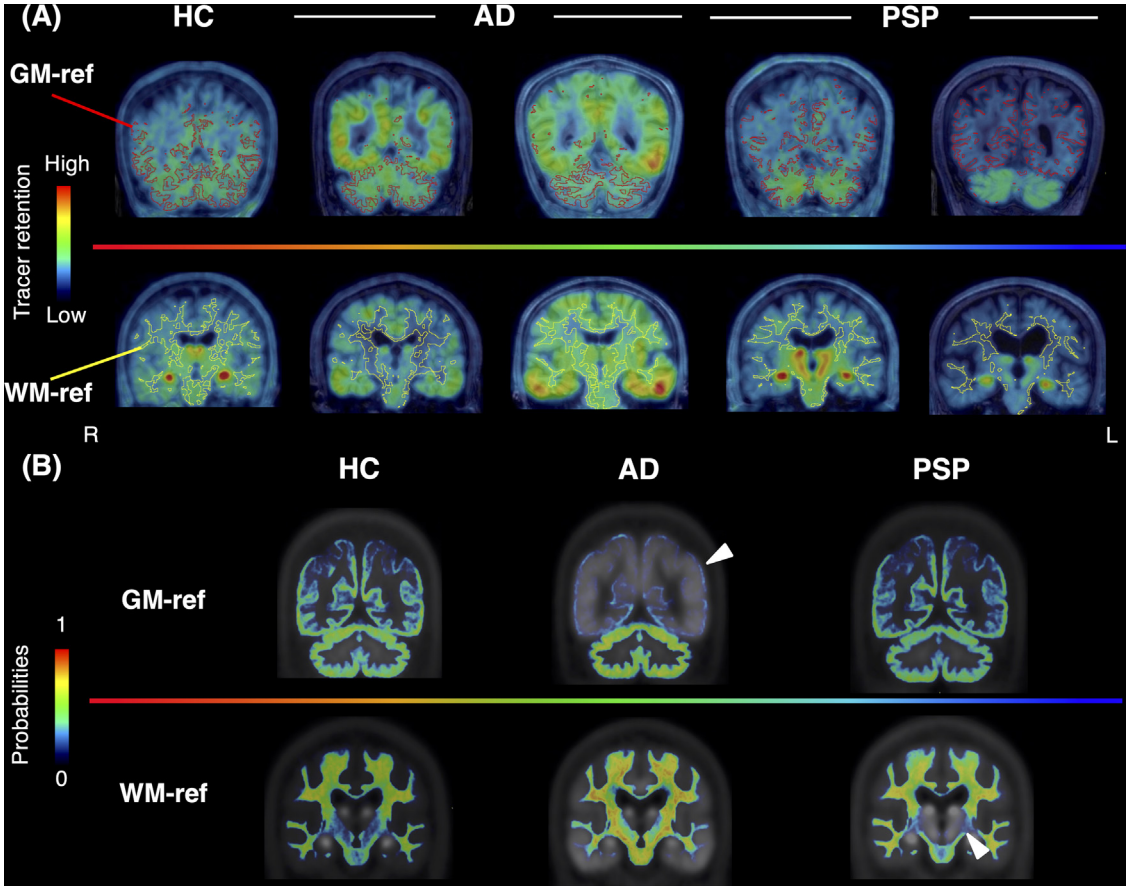

Fig. 2. Comparisons of topographies of GM-ref and WM-ref generated using histograms. (A) References generated by the histograms in representative cases of HCs and patients with AD and PSP. All PET images were co-registered T1-weighted MR images; red labeled regions demonstrate generated GM-ref (upper row); yellow labeled regions show WM-ref (lower row). (B) Averaged GM-ref and WM-ref in each diagnostic group on normalized spatial maps, reflecting the probability that each voxel is included in the reference tissue. Arrowheads point to the cerebral cortex of the AD group and basal ganglia of the PSP group, which exhibited lower probabilities of being selected as reference regions than those of the HC group, in agreement with the presumable high abundance of tau pathologies.

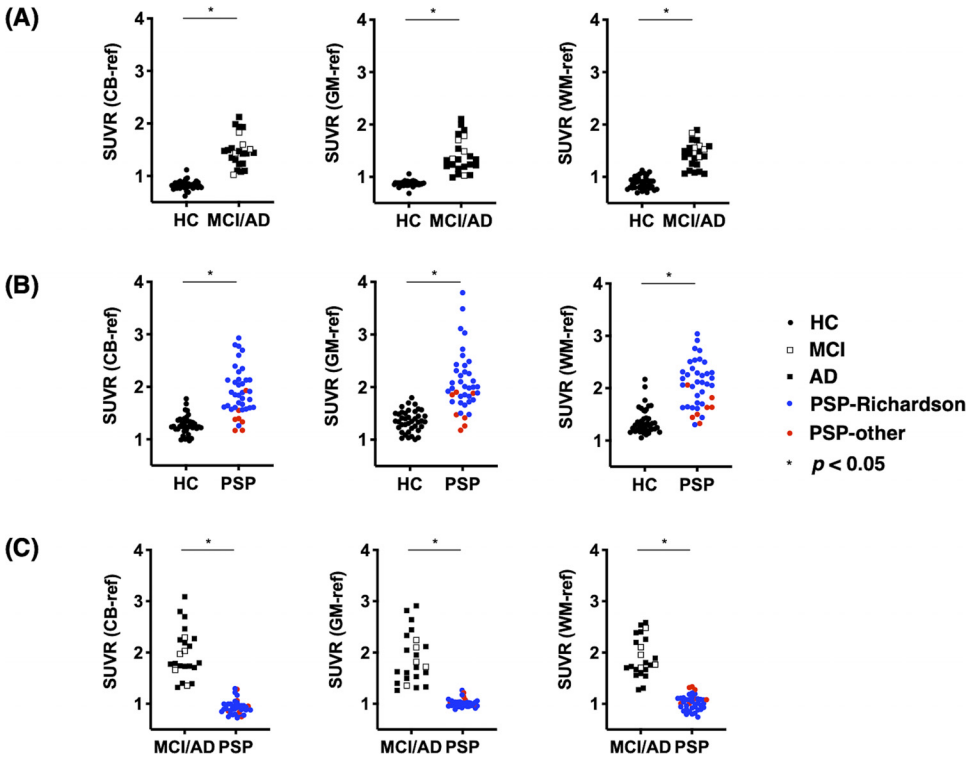

Fig. 3. Comparisons of the tracer binding in target regions quantified by each reference. Scatter plots show SUVR values of Braak V/VI (A), STN (B) and ITC (C) in the case of being quantified by each reference. The color of each dot indicates the clinical profile: black circles, (HC); white squares, (MCI); black squares, (AD); blue circles, (PSP-Richardson); red circles, (PSP-other). Asterisks indicate $P < 0.05$ by Mann-Whitney U test.

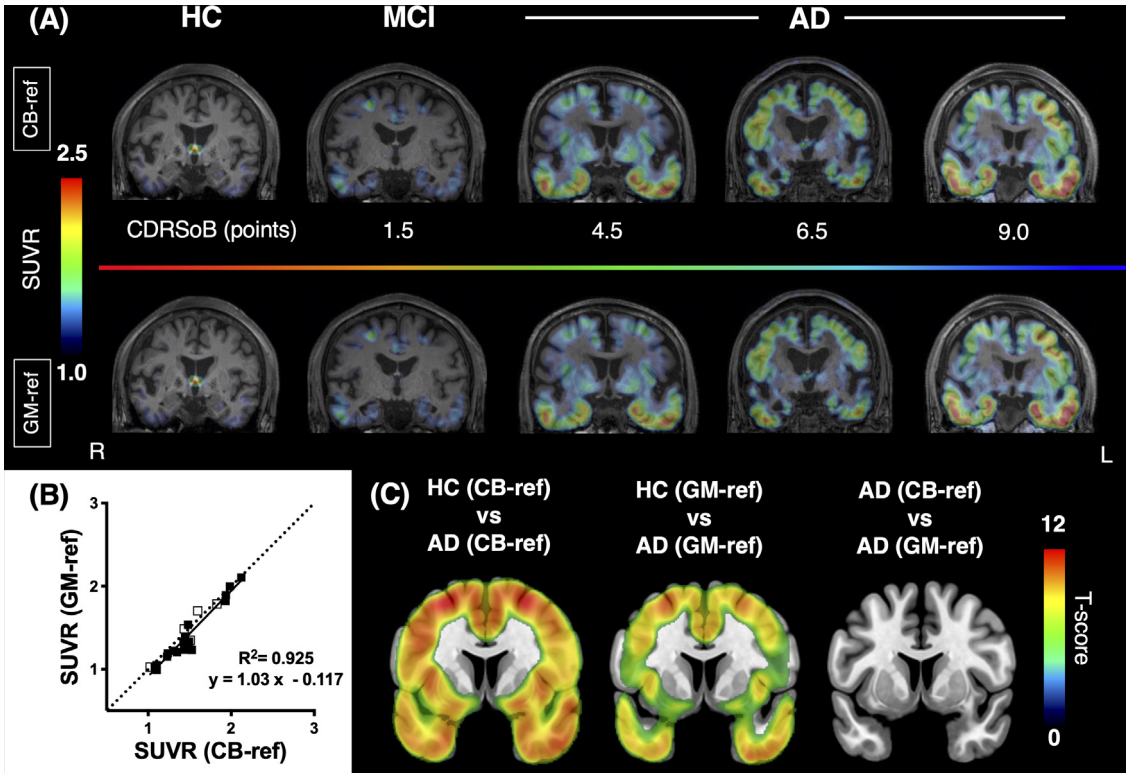

Fig. 4. Direct comparison of SUVRs quantified by CB-ref and GM-ref in HCs and AD patients. (A) SUVR parametric images quantified by CB-ref in the upper row and by GM-ref in the lower row are shown. Tau lesions are visualized with similar contrast to CB-ref from MCI to AD. (B) The scatterplot demonstrates a linear regression analysis. Black circles: (HC), white squares: (MCI), black squares: (AD). SUVR values are estimated from BraakV/VI VOI. (C) Statistical maps showing voxel-wise comparisons of SUVRs in the Montreal Neurological Institute coordinate space. Significantly increased accumulation in AD was detected in extensive areas of the cerebral cortex in each case estimated with CB-ref or GM-ref ($p < 0.05$, familywise error corrected at peak levels). There were no statistically significant differences between the two methods in AD.

3.3. Comparisons of imaging data yielded by CB-ref and GM-ref

We then compared parametric SUVR images generated with CB-ref and GM-ref, as WM-ref may not yield precise tau pathology measures because of aging correlations. The analyzes with CB-ref and GM-ref similarly captured spreading of the tracer retention from the medial and inferior temporal regions to the other neocortical areas along with cognitive declines in the continuum from MCI to AD (Fig. 4A). Moreover, SUVRs in the target VOIs estimated with GM-ref and CB-ref were in good agreement with each other in MCI and AD cases (Fig. 4B). Voxel-level comparisons with HCs showed higher t-scores in CB-ref cases than in GM-ref cases. Meanwhile, the comparison between each of the AD cases did not detect any voxels with a significant difference (Fig. 4C); the same results were also found using a paired *t*-test design (data not shown). By contrast, quantification using GM-ref detected tau depositions in PSP patients with higher SUVR than the analysis with CB-ref (Fig. 5A). Notably, tau accumulations primarily in the midbrain and left neocortical areas were undetectable with CB-ref but were clearly visualized with GM-ref in a PSP patient with aphasia (PSP-SL) (Fig. 5A). GM-ref yielded higher SUVR values in the target VOIs than CB-ref in these PSP cases, indicating high contrast for tau aggregates provided by GM-ref (Fig. 5B). Whole-brain analysis supported these findings, and also revealed a significant increase in tracer accumulation surrounding the cerebellum in GM-ref (Fig. 5C).

We also assessed individual SUVR images of patients with various clinical and/or neuropathological phenotypes of non-PSP FTLDs (Fig. 6). In a case with neuropathologically confirmed CBD, the assay with GM-ref captured tau depositions in the motor cortex and subcortical areas more sensitively than the use of CB-ref. Besides, GM-ref allowed imaging of tau pathologies with topologies characteristic of PSP and CBD in non-AD CBS and PNFA patients with higher contrast than CB-ref. Finally, SUVR images generated with CB-ref and GM-ref displayed high similarity in BvFTD patients with suspected or confirmed PiD neuropathology, presumably due to the lack of tau aggregates in the cerebellum.

4. Discussion

In the present work, we optimized the determination of reference tissue for the sensitive and precise PET detection of tau pathologies in various neurodegenerative dementias. This methodology improves the utility of the advantage of ^{18}F-PM-PBB3 as an imaging agent for AD and non-AD tau depositions. In addition to the conventional CB-ref placement, Gaussian fits to individual histograms of ^{18}F-PM-PBB3 retentions in GM and WM segments provided a range of radioligand uptakes for the extraction of voxels with a low likelihood of possessing tau deposits. Notably, GM-ref demonstrated robust diagnostic performance regardless of disease or aging, and allowed for accurate quantification at the individual level, especially in cases such as PSP and CBD where CB-ref could be contaminated with tau lesions. Accordingly, our findings validate the utilization of GM-ref for capturing and quantifying different types of tau accumulations in any of the brain regions, including the cerebellum.

The application of histograms enabled us to exclude regions that were likely to contain specific binding and to extract optimized reference regions regardless of the type of diseases (Kimura et al., 2016; Southekal et al., 2018). A vital issue in the histogram-based definition of reference voxels is the choice of an adequate mathematical model to describe the observed curves, as exemplified by monomodal and bimodal Gaussian fits. In the employment of our precedent tau PET probe, ^{11}C-PBB3, a relatively low dynamic range for the detection of specific binding components impeded the application of a bimodal fit to the ac-

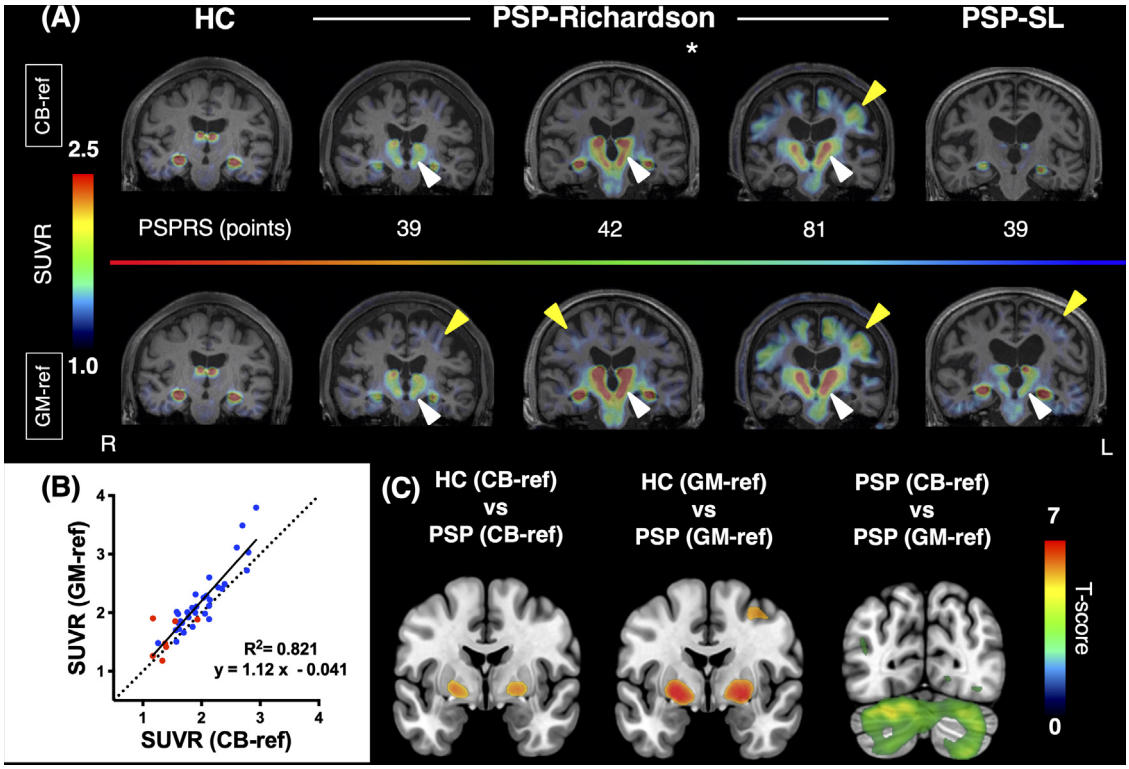

Fig. 5. Direct comparison of SUVRs quantified by CB-ref and GM-ref in HCs and PSP patients. (A) SUVR parametric images quantified by CB-ref in the upper row and by GM-ref in the lower row are shown. Tracer retention was increased and visualized in GM-ref compared to CB-ref in areas with well-known PSP pathology such as basal ganglia (white arrowheads) and motor cortex (yellow arrowheads). The asterisk image was obtained from a neuropathologically confirmed PSP patient. (B) The scatterplot demonstrates a linear regression analysis. Blue circles, (PSP-Richardson); red circles, (PSP with other clinical phenotypes). SUVR values are estimated from STN VOI. (C) Statistical maps showing voxel-wise comparisons of SUVRs in the Montreal Neurological Institute coordinate space. Significantly increased accumulation in PSP was detected in the basal ganglia in both cases with CB-ref and GM-ref, and also motor cortex in the case with GM-ref ($p < 0.05$, familywise error corrected at peak levels). There were also significant differences in the cerebellum between the two methods in PSP ($p < 0.001$, uncorrected at peak level).

quired image data (Maruyama et al., 2013; Kimura et al., 2016). By contrast, high contrasts for tau deposits produced by ^{18}F-PM-PBB3 have allowed clear separation between two histogram clusters representing voxels with and without noticeable tau pathologies, and voxels lacking PET-visible tau fibrils constitute the first, larger peak (Fig. 1A). Meanwhile, the two peaks can barely be discriminated in histograms of HCs burdened with few tau aggregates and PSP cases harboring low-grade tau depositions, justifying the use of a monomodal fit in these subjects (Fig. 1B). Moreover, the first peak may be small but distinguishable from the second peak in patients with advanced AD, and GM-ref extracted by the bimodal fitting resembled CB-ref (Fig. 1C).

An additional advantage of the current procedure over the previous method (Kimura et al., 2016) is the assignment of a radioligand uptake range for the selection of reference voxels in each individual without introducing average cutoff values determined in the HC group. The group-wise cutoff could vary in a manner dependent on PET scanners and image reconstruction algorithms, precluding the unification of tau measurements among different PET facilities. The circumvention of this drawback in the present workflow will therefore facilitate multicenter tau PET assessments of elderly subjects on a large scale.

In this study, the radioligand retentions in GM-ref were not susceptible to aging, while the retentions in WM-ref declined with aging. WM-ref had been reported to be valid in several amyloid and tau PET studies (Southekal et al., 2018; Chen et al., 2015; Landau et al., 2015), as its large size could be advantageous for reducing the statistical variability relative to CB-ref. In the meantime, non-specific retentions of these radioprobes in WM areas have been observed to vary among HCs partially in relation to aging (Baker et al., 2019; Moscoso et al., 2021). It is also noteworthy that even slight alterations of off-target tracer binding may lead to large variabilities of SUVRs in the use of WM-ref if the background (free) tracer retention in WM is very low. We also noted differences in the non-displaceable radioligand retention between CB-ref and GM-ref in the HC and PSP brains (Supplementary Fig. 3), implying lower non-displaceable retentions in the non-cerebellar GM areas than in the cerebellar GM. However, as mentioned above, these retentions in CB-ref and GM-ref were not altered with aging. Although the age-related reduction of non-displaceable radioligand binding in the white matter could arise from progressive declines of myelin components, molecular and histological substrates of this correlation are yet to be identified. In light of these observations, we consider GM-ref to be preferable to WM-ref for the quantification of tau deposits with this radioligand.

GM-ref also exhibited better diagnostic performance than CB-ref in patients with FTLD disorders, and particularly in those with putative and confirmed PSP and CBD pathologies. Indeed, PSP tau pathologies could involve the cerebellar dentate nucleus and adjacent WM from a relatively early stage (Kovacs et al., 2020; Williams et al., 2007). Similarly, tau lesions can be found in these areas of atypical or advanced CBD cases (Kouri et al., 2011; Ling et al., 2016; Shiozawa et al., 2000). Furthermore, tau inclusions in cerebellar GM Purkinje cells have also been detected in both PSP and CBD patients (Piao et al., 2002; Koga et al., 2016). Thus, the localization of these pathological tau aggregates could undermine the validity of CB-ref for the PET assessment of FTLD disorders. The histogram-based reference definition proposed here can exclude voxels with potential tau pathologies throughout the entire GM or WM, including the cerebellar regions, in an unbiased fashion. In fact, GM-ref was composed of extensive neocortical areas rather than the cerebellar sectors in consecutive PSP and CBD cases, along with CBS and PNFA patients suspected of having PSP or CBD pathologies, and low-grade tau

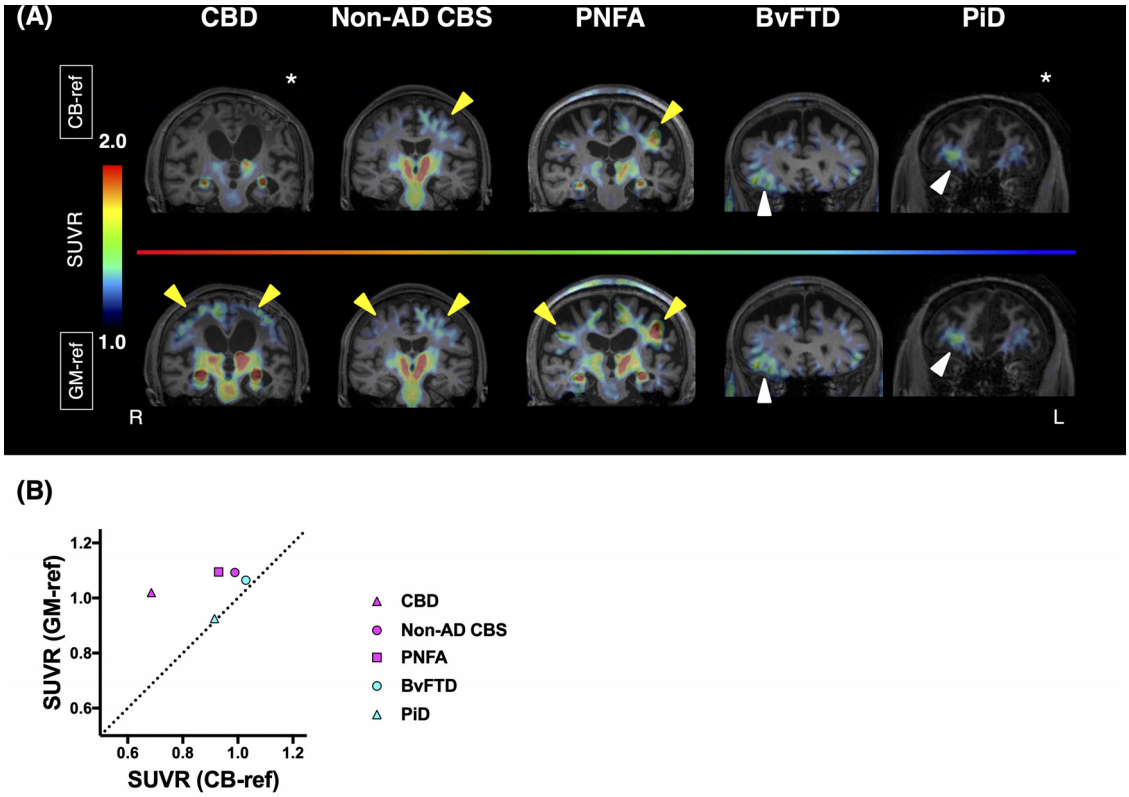

Fig. 6. Direct comparison of SUVRs quantified by CB-ref and GM-ref in other FTLD patients. (A) SUVR parametric images quantified by CB-ref in upper row and by GM-ref in lower row are shown. Tracer retention was increased and visualized in GM-ref compared to CB-ref in CBD, non-AD CBS, PNFA and patients, but it remained almost the same in BvFTD and PiD patients. Arrowheads indicate each target region: motor (yellow) and orbito (white) frontal cortices. Asterisked images were derived from neuropathologically confirmed patients. (B) Comparison of SUVR values quantified by CB-ref and GM-ref n each target region. Each target region was set at precentral cortex of CBD (magenta triangle), Non-AD CBS (magenta circle) and PNFA (magenta square) patients, and orbitofrontal cortex of BvFTD (light blue circle) and PiD (light blue triangle).

accumulations in neocortical structures of these subjects could be captured by using GM-ref but not CB-ref. By contrast, tau depositions in PiD patients were nearly equally detectable by applying GM-ref and CB-ref, in agreement with the lack of intense cerebellar tau lesions in this disorder.

GM-ref and CB-ref showed comparable diagnostic performance in discriminating AD cases from HCs. GM-ref showed a lower t-scores than CB-ref in voxel-level comparisons with HCs, which might be led by differences in non-displaceable retention in HCs according to comparisons between GM-ref and CB-ref in AD cases. Although the normalized spatial map of GM-ref suggested that reference voxels could be also extracted from cerebral cortex in AD, whose probabilities were quite low compared to cerebellar cortex. According to our workflow, which measures tracer accumulation in the reference region with probability weighting, the contribution of voxels from cerebral cortex would not be so substantial in the present dataset mainly consisting of AD dementia. At the same time, we also postulate that GM-ref can utilize a larger volume of brain areas than CB-ref in the assays of patients with prodromal and early AD, contributing to a gain in quantification stability. Although further investigation is still needed, this potential benefit would help sensitive detection of tau accumulations with low abundances in incipient AD.

Despite the demonstrated advantages of the current analytical method, several technical issues should be considered towards establishing a robust quantitative procedure. Firstly, the extracted reference voxels could spatially alter over the long term in a longitudinal assessment. Meanwhile, longitudinal instability has been noted in the conventional quantitative analysis using the cerebellum as a reference in AD (Young et al. 2021). As indicated elsewhere, this issue may be attributable to fluctuations of non-specific binding components (Moscoso et al. 2021). It is also likely that non-displaceable retentions of the tracer diminish over time due to aging- or neuropathology-associated hypoperfusion, while the cerebellum is less involved in these events. These processes may result in notable differences in the non-displaceable volume of distribution of the radioligand between the target regions and cerebellum. Therefore, we consider that the selection of optimal reference voxels at each time might rather avoid the influence of these tau-unrelated alterations, although further validation of this notion is still needed. Secondly, we defined GM and WM segments by performing erosions of $3 \times 3 \times 3$ neighboring voxels in consideration of the voxel size of MR images. Although erosion effects differed between through-plane and in-plane directions depending on the anisotropic voxel size, we confirmed that low-count boundary regions such as GM surface and CSF space were removed, and a sufficient number of GM and WM voxels remained in the histogram after erosion. Such verifications of the erosion extent would also be necessary in the application of different MRI voxel sizes. Thirdly, it is also probable that the number of Gaussian distributions incorporated in the fit alters in a longitudinal investigation as the Dice coefficient changes beyond the threshold. This issue may take place in a case with a progressive difference in the tracer retention between the first and second peaks, as exemplified by the advancement of AD tau burdens from incipient to full-blown levels. Therefore, there should be a tradeoff between the circumvention of influences of time-course changes in non-displaceable tracer retentions and possible instability of quantification originating from different model fits to the histogram. To examine the benefits and potential drawbacks of the current methodology, estimation of the radioligand binding using image data from a longitudinal cohort will be required. Furthermore, we may not be able to exclude the possibility that the histogram might be better described by

a trimodal Gaussian distribution model in a portion of individuals possessing two peaks for the specific binding components that reflect mild and severe tau burdens. There appeared no such cases in the present AD group since quantifications with CB-ref and GM-ref yielded almost identical SUVRs in target areas (Fig. 4). The feasibility of the current protocol will be further demonstrated by analyzing AD cases with low tau loads. Alternatively, a standard approach (e.g., applying a common reference region as a template) might be beneficial for reducing these variabilities in a longitudinal and multicenter setting. However, according to the comparison of GM-ref or WM-ref among the HC, AD, and PSP groups, there were no common regions to be employed as a reference in a standard approach (Fig. 2B). The cerebellum was included in GM-ref of HCs, AD patients, and some PSP cases but not in the rest of the PSP subjects. Furthermore, all WM areas showed a variable probability of being included in the reference tissue among the three diagnostic groups.

Despite these limitations, the newly developed workflow for the determination of reference tissue fortifies the utility of ^{18}F-PM-PBB3 for investigating a broad spectrum of neurodegenerative tauopathies with high contrast. The conjunction of the PET technology targeting diverse tau pathologies and the current quantitative procedure would facilitate the detection of tau lesions in a significant subset of the subjects, potentially offering insights into the etiology and neuropathological phenotypes of various neurodegenerative disorders.

Funding

This study was supported in part by AMED under Grant Numbers JP18dm0207018, JP19dm0207072, JP18dk0207026, JP19dk0207049, 21wm0425015h0001, 21ek0109474h0002 and 20356533, by MEXT/JSPS KAKENHI Grant Numbers JP16H05324, JP18K07543, and JP22K15776, by JST Grant Numbers JPMJCR1652 and JPMJMS2024, and by Biogen Idec Inc. and APRINOIA Therapeutics.

Declaration of Competing Interest

Hitoshi Shimada, Ming-Rong Zhang, and Makoto Higuchi hold patents on compounds related to the present report (JP 5422782/EP 12 884 742.3/CA2894994/HK1208672).

Credit authorship contribution statement

Kenji Tagai: Conceptualization, Methodology, Formal analysis, Writing – original draft. **Yoko Ikoma:** Conceptualization, Methodology, Formal analysis, Writing – original draft. **Hironobu Endo:** Conceptualization, Methodology. **Oiendrila Bhowmik Debnath:** Conceptualization, Methodology. **Chie Seki:** Conceptualization, Methodology. **Kiwamu Matsuoka:** Data curation. **Hideki Matsumoto:** Data curation. **Masaki Oya:** Data curation. **Kosei Hirata:** Data curation. **Hitoshi Shinotoh:** Data curation. **Keisuke Takahata:** Data curation. **Shin Kurose:** Data curation. **Yasunori Sano:** Data curation. **Maiko Ono:** Conceptualization, Methodology. **Hitoshi Shimada:** Data curation. **Kazunori Kawamura:** Supervision. **Ming-Rong Zhang:** Supervision. **Yuhei Takado:** Conceptualization, Writing – review & editing, Funding acquisition, Supervision. **Makoto Higuchi:** Conceptualization, Writing – review & editing, Funding acquisition, Supervision.

Data Availability

Data will be made available on request.

Acknowledgments

The authors thank all patients and their caregivers for participation in this study, as well as clinical research coordinators, PET and MRI operators, radiochemists, and research ethics advisers at QST for their assistance with the current projects. We thank APRINOIA Therapeutics for kindly sharing a precursor of ^{18}F-PM-PBB3. The authors acknowledge support with the recruitment of patients by Shunichiro Shinagawa and Masahiro Shigeta at the Department of Psychiatry, Jikei University School of Medicine; Shigeki Hirano at the Department of Neurology, Chiba University; Taku Hatano, Yumiko Motoi, and Shinji Saiki at the Department of Neurology, Juntendo University School of Medicine; Ikuko Aiba at the Department of Neurology, National Hospital Organization Higashinagoya National Hospital; Yasushi Shiio and Tomonari Seki at the Department of Neurology, Tokyo Teishin Hospital; Hisaomi Suzuki at the National Hospital Organization Shimofusa Psychiatric Medical Center.

Supplementary materials

Supplementary material associated with this article can be found, in the online version, at doi:10.1016/j.neuroimage.2022.119763.

References

Arima, K., 2006. Ultrastructural characteristics of tau filaments in tauopathies: immuno–electron microscopic demonstration of tau filaments in tauopathies. Neuropathology 26 (5), 475–483.

Armstrong, M.J., Litvan, I., Lang, A.E., Bak, T.H., Bhatia, K.P., Borroni, B., et al., 2013. Criteria for the diagnosis of corticobasal degeneration. Neurology 80 (5), 496–503.

Baker, S.L., Harrison, T.M., Maass, A., La Joie, R., Jagust, W.J, 2019. Effect of off-target binding on (18)F-flortaucipir variability in healthy controls across the life span. J. Nucl. Med. 60 (10), 1444–1451.

Barret, O., Alagille, D., Sanabria, S., Comley, R.A., Weimer, R.M., Borroni, E., et al., 2017. Kinetic modeling of the tau PET tracer (18)F-AV-1451 in human healthy volunteers and alzheimer disease subjects. J. Nucl. Med. 58 (7), 1124–1131.

Buee, L., Bussiere, T., Buee-Scherrer, V., Delacourte, A., Hof, P.R., 2000. Tau protein isoforms, phosphorylation and role in neurodegenerative disorders. Brain Res. Brain Res. Rev. 33 (1), 95–130.

Chen, K., Roontiva, A., Thiyyagura, P., Lee, W., Liu, X., Ayutyanont, N., et al., 2015. Improved power for characterizing longitudinal amyloid-beta PET changes and evaluating amyloid-modifying treatments with a cerebral white matter reference region. J. Nucl. Med. 56 (4), 560–566.

Delacourte, A., 2005. Tauopathies: recent insights into old diseases. Folia Neuropathol. 43 (4), 244–257.

Endo, H., Shimada, H., Sahara, N., Ono, M., Koga, S., Kitamura, S., et al., 2019. *In vivo* binding of a tau imaging probe, [(11) C]PBB3, in patients with progressive supranuclear palsy. Mov. Disord. 34 (5), 744–754.

Gorno-Tempini, M.L., Hillis, A.E., Weintraub, S., Kertesz, A., Mendez, M., Cappa, S.F., et al., 2011. Classification of primary progressive aphasia and its variants. Neurology 76 (11), 1006–1014.

Hanley, J.A., McNeil, B.J., 1983. A method of comparing the areas under receiver operating characteristic curves derived from the same cases. Radiology 148 (3), 839–843.

Hoglinger, G.U., Respondek, G., Stamelou, M., Kurz, C., Josephs, K.A., Lang, A.E., et al., 2017. Clinical diagnosis of progressive supranuclear palsy: the movement disorder society criteria. Mov. Disord. 32 (6), 853–864.

Kimura, Y., Endo, H., Ichise, M., Shimada, H., Seki, C., Ikoma, Y., et al., 2016. A new method to quantify tau pathologies with (11)C-PBB3 PET using reference tissue voxels extracted from brain cortical gray matter. EJNMMI Res. 6 (1), 24.

Klein, A., Tourville, J., 2012. 101 labeled brain images and a consistent human cortical labeling protocol. Front. Neurosci. 6, 171.

Koga, S., Josephs, K.A., Ogaki, K., Labbe, C., Uitti, R.J., Graff-Radford, N., et al., 2016. Cerebellar ataxia in progressive supranuclear palsy: an autopsy study of PSP-C. Mov. Disord. 31 (5), 653–662.

Kouri, N., Murray, M.E., Hassan, A., Rademakers, R., Uitti, R.J., Boeve, B.F., et al., 2011. Neuropathological features of corticobasal degeneration presenting as corticobasal syndrome or Richardson syndrome. Brain 134 (Pt 11), 3264–3275.

Kovacs, G.G., Lukic, M.J., Irwin, D.J., Arzberger, T., Respondek, G., Lee, E.B., et al., 2020. Distribution patterns of tau pathology in progressive supranuclear palsy. Acta Neuropathol. 140 (2), 99–119.

Kuwabara, H., Comley, R.A., Borroni, E., Honer, M., Kitmiller, K., Roberts, J., et al., 2018. Evaluation of (18)F-RO-948 PET for quantitative assessment of tau accumulation in the human brain. J. Nucl. Med. 59 (12), 1877–1884.

Landau, S.M., Fero, A., Baker, S.L., Koeppe, R., Mintun, M., Chen, K., et al., 2015. Measurement of longitudinal beta-amyloid change with 18F-florbetapir PET and standardized uptake value ratios. J. Nucl. Med. 56 (4), 567–574.

Leuzy, A., Chiotis, K., Lemoine, L., Gillberg, P.G., Almkvist, O., Rodriguez-Vieitez, E., et al., 2019. Tau PET imaging in neurodegenerative tauopathies-still a challenge. Mol. Psychiatry 24 (8), 1112–1134.

Ling, H., Kovacs, G.G., Vonsattel, J.P., Davey, K., Mok, K.Y., Hardy, J., et al., 2016. Astrogliopathy predominates the earliest stage of corticobasal degeneration pathology. Brain 139 (Pt 12), 3237–3252.

Maruyama, M., Shimada, H., Suhara, T., Shinotoh, H., Ji, B., Maeda, J., et al., 2013. Imaging of tau pathology in a tauopathy mouse model and in Alzheimer patients compared to normal controls. Neuron 79 (6), 1094–1108.

McKhann, G., Drachman, D., Folstein, M., Katzman, R., Price, D., Stadlan, E.M., 1984. Clinical diagnosis of Alzheimer's disease: report of the NINCDS-ADRDA work group under the auspices of department of health and human services task force on Alzheimer's disease. Neurology 34 (7), 939–944.

Moscoso, A., Grothe, M.J., Scholl, M., 2021. Alzheimer's disease neuroimaging I. Reduced [(18)F]flortaucipir retention in white matter hyperintensities compared to normal-appearing white matter. Eur. J. Nucl. Med. Mol. Imaging 48 (7), 2283–2294.

Mueller, A., Bullich, S., Barret, O., Madonia, J., Berndt, M., Papin, C., et al., 2020. Tau PET imaging with (18)F-PI-2620 in patients with Alzheimer disease and healthy controls: a first-in-humans study. J. Nucl. Med. 61 (6), 911–919.

Ossenkoppele, R., Rabinovici, G.D., Smith, R., Cho, H., Scholl, M., Strandberg, O., et al., 2018. Discriminative accuracy of [18F]flortaucipir positron emission tomography for alzheimer disease vs other neurodegenerative disorders. JAMA 320 (11), 1151–1162.

Pascoal, T.A., Shin, M., Kang, M.S., Chamoun, M., Chartrand, D., Mathotaarachchi, S., et al., 2018. *In vivo* quantification of neurofibrillary tangles with [(18)F]MK-6240. Alzheimers Res. Ther. 10 (1), 74.

Petersen, R.C., Smith, G.E., Waring, S.C., Ivnik, R.J., Tangalos, E.G., Kokmen, E., 1999. Mild cognitive impairment: clinical characterization and outcome. Arch. Neurol. 56 (3), 303–308.

Piao, Y.S., Hayashi, S., Wakabayashi, K., Kakita, A., Aida, I., Yamada, M., et al., 2002. Cerebellar cortical tau pathology in progressive supranuclear palsy and corticobasal degeneration. Acta Neuropathol. 103 (5), 469–474.

Rascovsky, K., Hodges, J.R., Knopman, D., Mendez, M.F., Kramer, J.H., Neuhaus, J., et al., 2011. Sensitivity of revised diagnostic criteria for the behavioural variant of frontotemporal dementia. Brain 134 (Pt 9), 2456–2477.

Shi, Y., Zhang, W., Yang, Y., Murzin, A.G., Falcon, B., Kotecha, A., et al., 2021. Structure-based classification of tauopathies. Nature 598 (7880), 359–363.

Shinotoh, H., Shimada, H., Kokubo, Y., Tagai, K., Niwa, F., Kitamura, S., et al., 2019. Tau imaging detects distinctive distribution of tau pathology in ALS/PDC on the Kii Peninsula. Neurology 92 (2), e136–ee47.

Shiozawa, M., Fukutani, Y., Sasaki, K., Isaki, K., Hamano, T., Hirayama, M., et al., 2000. Corticobasal degeneration: an autopsy case clinically diagnosed as progressive supranuclear palsy. Clin. Neuropathol. 19 (4), 192–199.

Southekal, S., Devous, M.D., Kennedy, I., Navitsky, M., Lu, M., Joshi, A.D., et al., 2018. Flortaucipir F 18 quantitation using parametric estimation of reference signal intensity. J. Nucl. Med. 59 (6), 944–951.

Tagai, K., Ono, M., Kubota, M., Kitamura, S., Takahata, K., Seki, C., et al., 2021. High–contrast *in vivo* imaging of tau pathologies in Alzheimer's and non-Alzheimer's disease tauopathies. Neuron 109 (1) 42-58 e8.

Takahata, K., Kimura, Y., Sahara, N., Koga, S., Shimada, H., Ichise, M., et al., 2019. PET-detectable tau pathology correlates with long-term neuropsychiatric outcomes in patients with traumatic brain injury. Brain 142 (10), 3265–3279.

Villemagne, V.L., Dore, V., Burnham, S.C., Masters, C.L., Rowe, C.C., 2018. Imaging tau and amyloid-beta proteinopathies in Alzheimer disease and other conditions. Nat. Rev. Neurol. 14 (4), 225–236.

Williams, D.R., Holton, J.L., Strand, C., Pittman, A., de Silva, R., Lees, A.J., et al., 2007. Pathological tau burden and distribution distinguishes progressive supranuclear palsy-parkinsonism from Richardson's syndrome. Brain 130 (Pt 6), 1566–1576.

Young, C.B., Landau, S.M., Harrison, T.M., Poston, K.L., Mormino, E.C., 2021. Influence of common reference regions on regional tau patterns in cross-sectional and longitudinal [^{18}F]-AV-1451 PET data. NeuroImage 243, 118553. doi:10.1016/j.neuroimage.2021.118553.

Zhang, H., Wang, M., Lu, J., Bao, W., Li, L., Jiang, J., et al., 2021. Parametric estimation of reference signal intensity for semi-quantification of tau deposition: a flortaucipir and [(18)F]-APN-1607 study. Front. Neurosci. 15, 598234.